

# **Results of the IFCI 6.0 Assessment: Calculations of MAGICO-701, MIXA-6, KROTOS-26 and 38, and Single-Drop Oxidation Experiments**

A. W. Reed, M. F. Young, and R. C. Schmidt  
Sandia National Laboratories

## **Abstract**

Version 6.0 of the IFCI code is being assessed by comparing predictions against the results of the MAGICO-701, MIXA-6, KROTOS-26, KROTOS-38, and single-drop oxidation experiments. To date, all but the KROTOS experiments have been simulated with some level of success. Agreement with the MAGICO-701 experiment was good but was limited somewhat by the inherent problem of numerical diffusion. Results of the MIXA-6 calculations were comparable to those of CHYMES, but clearly displayed the need for an inter-cell radiation transport model in IFCI. The extent of the single-drop oxidation was correctly predicted within 33%, which reflects the oxidation correlation used within IFCI.

Attempts to model the coarse mixing stage of the KROTOS experiments are still hampered by numerical stability problems associated with subcooling. The problem has been associated with the pressure solution in cells containing small quantities of vapor and some quantity of fuel, but further study is necessary to correct the problem.

In order to demonstrate the capability of IFCI to model acoustic and detonation waves, the KROTOS-26 trigger pulse was modeled using an assumed coarse mixing configuration. The response of three of the transducers located in the solid-water section corresponded well with the data. However, the calculation indicated that the pressure wave damped out in the multi-phase region which contained 20% vapor. Further examination of the detonation data suggested that the coarse mixing region might be 2-dimensional. A successful coarse mixing calculation will be necessary in order to fully understand the apparent anomalies in the KROTOS-26 data.

## Table of Contents

1. Introduction	1
2. MAGICO-701	2
2.1 Experiment Geometry and Results	2
2.2 Comparison of IFCI Predictions with Experimental Measurements	2
3. MIXA-6	6
3.1 Experiment Geometry	6
3.2 Incorporation of Pressurization in IFCI	6
3.3 Comparison of IFCI Predictions with Experimental Measurements	9
4. KROTOS-26 and KROTOS-38	12
4.1 Experiment Geometry	12
4.2 IFCI Calculations	12
5. Single Droplet Oxidation Experiment	18
6. Conclusions	21
7. References	23
Appendix A: Studies of Numerical Diffusion and Numerical Input Parameters in IFCI	25
Appendix B: Potential Impact of Pressurization in MIXA-6	30
Appendix C: Derivation of Inflow Boundary Conditions for MIXA-6	31
Appendix D: Estimate of Thermal Radiation from Falling Melt to the Water	33
Appendix E: Derivation of the Inflow Boundary for Krotos 38	36
Appendix F: Notes on Procedures	38
Appendix G: Input deck to MAGICO-701	40
Appendix H: Input deck to MIXA-6	48
Appendix I: Input deck to KROTOS-26	54
Appendix J: Input deck for KROTOS-38	62
Appendix K: Input deck for Iron Oxidation Experiment	67

## List of Figures

Figure 1	Schematic of MAGICO-701 as Modeled in IFCI.....	2
Figure 2	Distribution of Particulate in Water at Centerline (0.23 sec).....	3
Figure 3	Advancement of the Front of Hot Particles (Threshold=0.0005).....	4
Figure 4	Average Steam Volume Fraction in the Particle Region (Threshold=0.0005).....	4
Figure 5	Advance of the Front of Hot Particles (Threshold=0.005).....	5
Figure 6	Average Steam Volume Fraction in the Particle Region (Threshold=0.005).....	5
Figure 7	Schematic of MIXA-6 as Modeled in IFCI.....	6
Figure 8	The Measured Pressure in the Gas Space for Experiment MIXA-6.....	7
Figure 9	The Transient Steaming Rate: A Comparison of the Calculated Values with the Experimental Data .....	7
Figure 10	Pressure-Drop/Flow-Rate Curve for the MIXA-6 Experiment.....	8
Figure 11	Steam Production Rate Calculated by IFCI.....	10
Figure 12	Schematic of KROTOS-26 as Modeled in IFCI.....	13
Figure 13	IFCI Mixing Predictions for KROTOS-26 (1.48 sec, no condensation).....	14
Figure 14	Post-Triggering Pressure Transducer Readings from KROTOS-26.....	15
Figure 15	Predicted Response to the Detonation Trigger .....	16
Figure 16	IFCI Oxidation Predictions .....	19
Figure 17	Iron/Oxygen Phase Diagram .....	20
Figure 18	MIXA-6 Melt Concentration Profiles Calculated by Coarse Mesh (10 nodes in the water) at 0.00, 0.14, and 0.24 sec .....	25
Figure 19	Effect of Mesh Refinement in MIXA-6 on Numerical Diffusion.....	26
Figure 20	"Melt" Concentration Profiles Calculated by the Finest Mesh (160 nodes in the water) at 0.00, 0.14, and 0.24 sec .....	27
Figure 21	Effect of Mesh Refinement in MAGICO-701 on Numerical Diffusion.....	28
Figure 22	Calculated Steam Production Rate Due to Radiation from Falling Melt.....	34
Figure 23	Schematic of the Crucible / Jet Configuration.....	36
Figure 24	Computed Jet Exit Velocity as a Function of Time.....	37

## List of Tables

Table 1	MAGICO-701 Experiment Parameters.....	2
Table 2	The Fraction of Thermal Energy Absorbed as a Function of Melt Temperature and Path-Length.....	11
Table 3	Pressure Transducer Locations .....	12
Table 4	KROTOS Experiment Parameters.....	12
Table 5	Initial Conditions and Results for the Single Droplet Test.....	18

## 1. Introduction

The Integrated Fuel-Coolant Interaction (IFCI) code is designed to model the mixing of molten nuclear reactor materials with reactor coolant (water). It is designed to handle, with varying degrees of empiricism, the four stages of fuel-coolant interactions: coarse mixing, triggering, detonation propagation, and hydrodynamic expansion. IFCI contains models for boiling rates, flow regimes, dynamic melt fragmentation, surface tracking, subcooling effects, melt oxidation, triggering, and propagation of the shock. These phenomena are essential to the modeling of fuel/coolant interactions. IFCI is under development at Sandia National Laboratories (SNL) and is sponsored by the United States Nuclear Regulatory Commission, Office of Nuclear Regulatory Research (USNRC/RES).

In order to assess the current version of the code, predictions made by IFCI were compared to five experiments from four different experiment series: MAGICO-701, MIXA-6, KROTOS-26, KROTOS-38, and a single-drop oxidation experiment. While these five experiments are but a small number of those that have been conducted, they represent a broad range of phenomena. The MAGICO and MIXA experiments focused only on coarse mixing phenomena. The MAGICO experiments utilized hot, stainless steel spheres heated to relatively low temperatures and measured the steam volume fraction during mixing. The MIXA experiments used molten urania at high temperature and measured the steam generation rate. The KROTOS-26 and 38 experiments attempted to examine the properties of propagation by artificially triggering an explosive reaction. The single-drop oxidation experiment measured the hydrogen generation rate of a single molten steel drop.

This document presents the results of the work conducted to date. Direct comparisons between experimental data and IFCI calculations are presented for the MAGICO-701, MIXA-6, and drop oxidation experiments. Progress on the KROTOS-26 and 38 experiments remains constrained by numerical stability difficulties. Insights on the KROTOS-26 experiment are presented.

## 2. MAGICO-701

### 2.1 Experiment Geometry and Results

The MAGICO experiments [1] were designed to measure the vapor volume fraction in the region of the melt without the complicating phenomenon of particle breakup. This was accomplished by dropping hot steel (SS316) balls from a perforated plate into a pool of water at the saturation temperature. The water was contained in a rectangular vessel (406 mm square by 355 mm high) made of tempered glass. The progression of the hot particles downward in the pool and the resulting increase in the water level were recorded by video camera. The video indicated that there was little radial spreading of the boiling region. Based upon this observation, the average vapor volume fraction ( $\bar{\alpha}_{vapor}$ ) was computed from the equation:

$$\bar{\alpha}_{vapor} = \frac{(h - h_0)}{L_{front}} \left( \frac{d_{pool}}{d_{pour}} \right)^2 \quad (2-1)$$

where  $h$  is the water height at the outer circumference of the pool, and  $L_{front}$  is the penetration depth of the steel balls in the pool. This equation ignores the volume fraction of the steel balls, which is estimated by the authors [1] to be less than 2%.

A number of combinations of initial water depths ( $h_0$ ), particle temperatures and diameters, and pour diameters ( $d_{pour}$ ) defined the test series. The MAGICO 701 test had the parameters listed in Table 1. The ball velocity at the base of the perforated plate was measured at 72 cm/second. The ball volume fraction at the perforated plate was measured at 1.87 %.

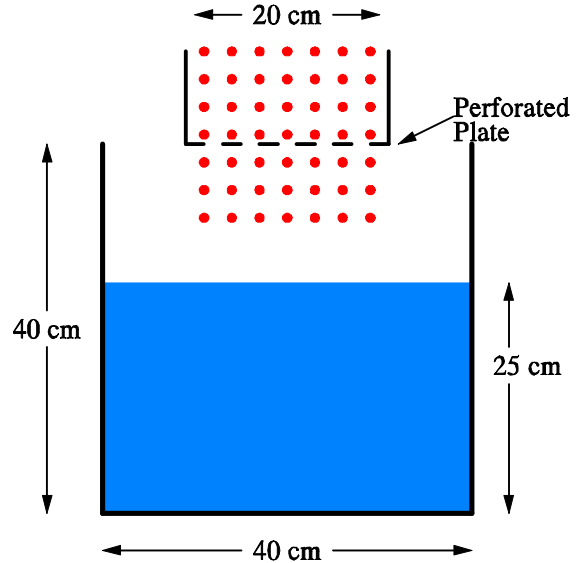


**Figure 1** Schematic of MAGICO-701 as Modeled in IFCI

**Table 1** MAGICO-701 Experiment Parameters

Ball Temperature	550 C
Ball Diameter	2.4 mm
Pool Depth	25 cm
Free fall Distance	15 cm

### 2.2 Comparison of IFCI Predictions with Experimental Measurements

The MAGICO-701 experiment domain was modeled as a right circular cylinder, having an outer radius of 20 cm. and a height of 40 cm. In order to check for numerical diffusion (Appendix A), three mesh resolutions were used to model the MAGICO-701 experiment. The coarse, medium, and fine meshes contained 32, 64, and 104 axial cells, respectively. All of the meshes contained

10 radial cells. The cell heights and radial lengths were uniform throughout the domain. The entry of steel balls into the experiment was modeled by a flux condition at the top half of the domain. Steam was allowed to escape from the outer three cells at the top of the domain. The input deck for the MAGICO-701 model is located in Appendix G.

The distribution of hot particles in the water 0.23 seconds after initial entry is shown in Figure 2. The plot shows the predicted volume fraction of steel balls at the centerline at 0.23 seconds after initial impact with the water surface. The volume fraction is approximately 2 % near the surface of the water. The volume fraction starts to decline at an elevation of about 15 cm to a value of about 0.35 % at an elevation of 5 cm.

The plot illustrates the differences in predictions between the coarse, medium, and fine meshes. The medium and fine meshes show a particle front that is on the verge of touching the bottom of the container. The coarse mesh shows a front that has already reached the container

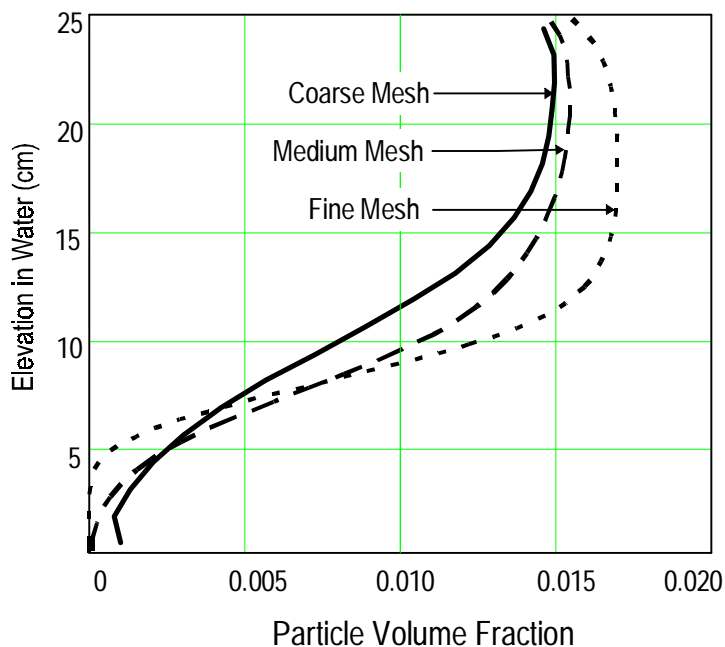


**Figure 2 Distribution of Particulate in Water at Centerline (0.23 sec)**

bottom and the particulate beginning to accumulate. The differences between the predictions are most likely due to numerical diffusion. (Appendix A)

Particle motion is not, in of itself, diffusive in nature. However, the use of an Eulerian (stationary) grid to model particle motion adds an artificial diffusive component to the numerical solution. This results in the smeared leading edge that is evident in Figure 2. This means that the analyst must choose a threshold volume fraction to define the calculated particle front. The value for the threshold volume fraction is based upon the full range of the volume fraction and the shape of the spatial profile. Figure 2 shows that the maximum predicted particle volume fraction is between 0.015 and 0.017. For this analysis, threshold values of 0.0005 and 0.005 were chosen and used to calculate the advancement of the particle front. The difference between the two calculations (based upon 0.0005 and 0.005) is a measure of the uncertainty in the calculation due to numerical diffusion.

Figure 3 compares the measured front advancement with the IFCI predictions using a threshold volume fraction of 0.0005. The decreasing slope of the data indicates a front that slows somewhat with increasing time. Although the data does not show the exact time when the front arrives at the container bottom, extrapolation of the data suggests a transit time of approximately 0.35 seconds. IFCI predicts the location of the front accurately at early times, but does not

exhibit the slowing of the front to the same degree as the data. The effect of meshing is evident in the predictions. The coarse, medium, and fine meshes show total transit times of 0.22, 0.25, and 0.28 seconds, respectively. Increasingly finer meshes improve the calculation of the total transit time. None of the meshes produce the decreasing slope seen in the data.

The average vapor volume fraction in the region behind the advancing front is shown in Figure 4. The data shows an increase to approximately 0.28 % at about 0.2 sec, after which it remains approximately constant or declines somewhat. The IFCI predictions come reasonably close to the experimental data up through the calculated sphere settling time. The coarse mesh underpredicts the data up until the predicted transit time of 0.22 seconds (shown as a vertical dotted line). The medium and fine meshes are progressively closer to the data over the predicted transit times of 0.25 and 0.28 seconds (also shown as vertical dotted lines)

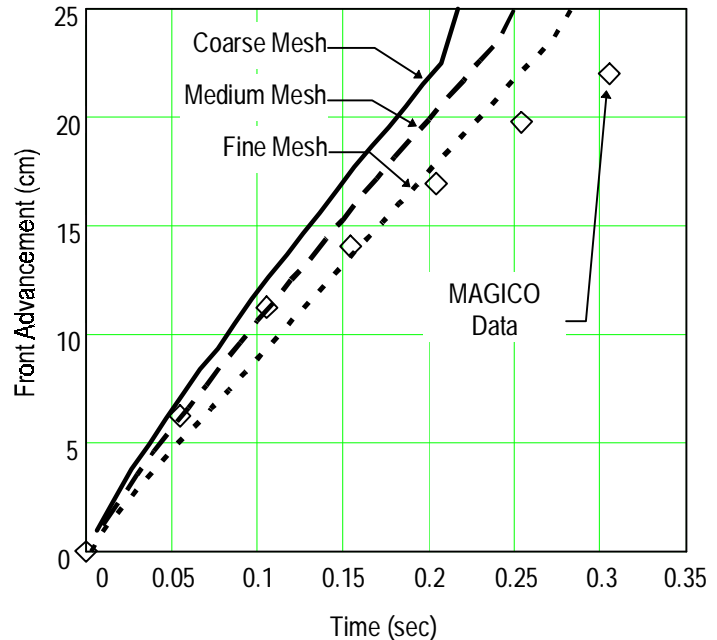


**Figure 3 Advancement of the Front of Hot Particles (Threshold=0.0005)**

Figure 5 shows the predicted front advancement for a front threshold value of 0.005. The increase in the selected threshold volume fraction improves the comparison between predicted and measured front position, especially at latter times. This same increase in chosen threshold value raises slightly the predicted average steam volume fraction within the melt zone (Figure 6) and decreases the mesh-dependence.

It should be emphasized that the differences between Figure 3 and Figure 5 and between Figure 4 and Figure 6 are a result of interpreting the same computer run. The source of the problem is the diffusive nature of the numerical approach used to calculate

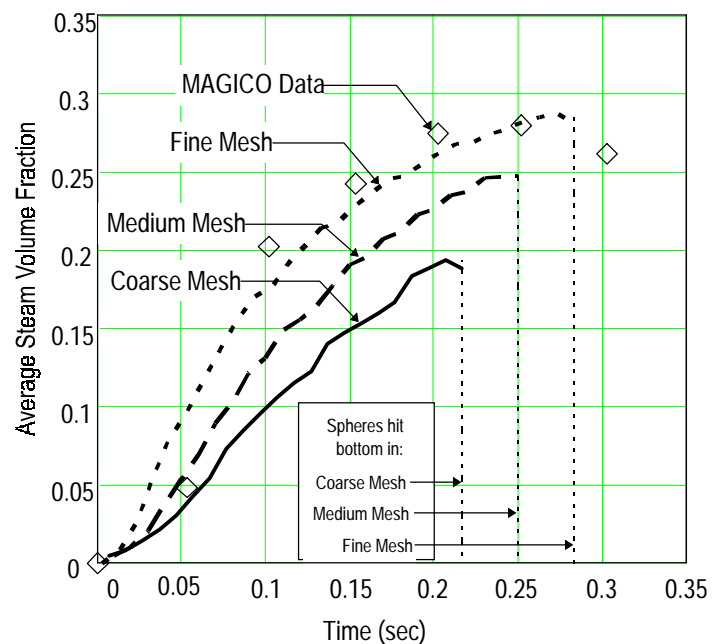


**Figure 4 Average Steam Volume Fraction in the Particle Region (Threshold=0.0005)**

particle convection. This problem is not unique to IFCI, and should be found in similar codes which use an Eulerian grid and donor-cell differencing.

While the choice of the threshold value for defining the particle front is somewhat subjective, it is believed that the range of threshold values examined in this analysis is reasonable. Within this range, it appears that IFCI predictions for particle front advancement and average vapor fraction are reasonably close to the measured data. However, the demonstrated dependence of the prediction upon the grid resolution suggests that finer meshes are likely to produce more accurate predictions.

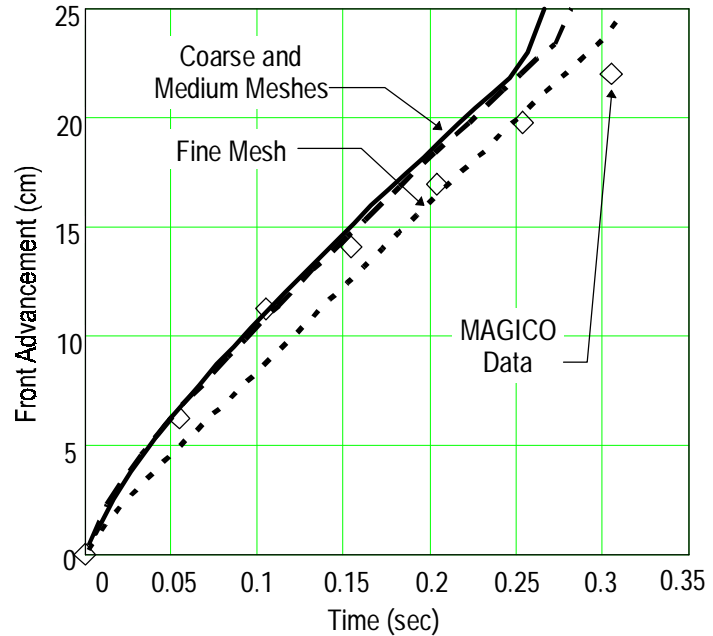


**Figure 5 Advance of the Front of Hot Particles (Threshold=0.005)**

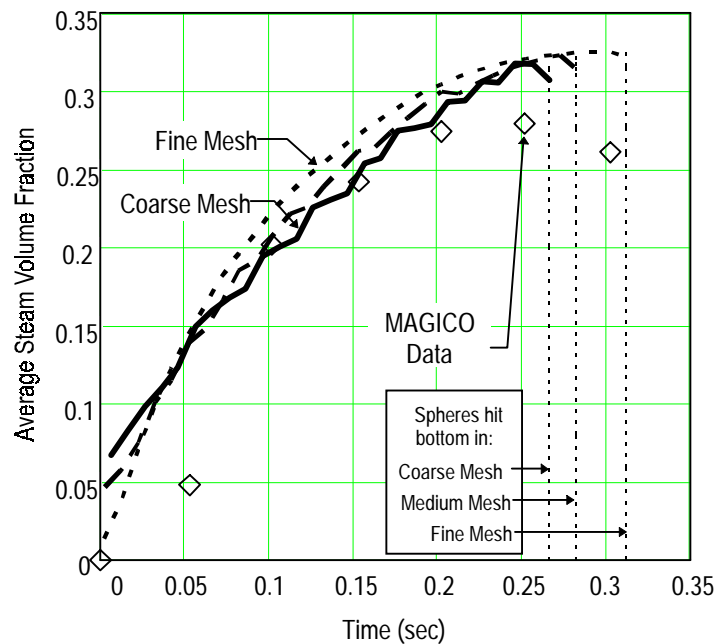


**Figure 6 Average Steam Volume Fraction in the Particle Region (Threshold=0.005)**



### 3. MIXA-6

#### 3.1 Experiment Geometry

The MIXA experiments [2,3] were designed to measure steam production rate during the coarse mixing stage of fuel/coolant interactions. A molten fuel simulant (81%  $\text{UO}_2$ , 19% Mo) was poured over a grid of carbon bars, which produced 16 streams of molten material. These streams broke up into droplets having a diameter of approximately 6 mm. A steel tube having an inside diameter of 122 mm was placed immediately below the carbon bars to constrain the lateral spreading of the melt. The length of the tube was varied between individual experiments. In the MIXA-6 experiment, the tube length was 480 mm.

The molten material (3.0 kg for MIXA-6) was released into a pool of water from an elevation of about 1 m. The water pool was square in cross section (0.37 m each side) with a depth of 0.6 m. The water was initially at saturation temperature at a pressure of 1 atmosphere. The volumetric steam flow rate was measured by a vortex flowmeter connected to the top of the experiment chamber by a 100 mm diameter vent line. Pressure in the gas region of the chamber was measured using strain gauge pressure transducers.

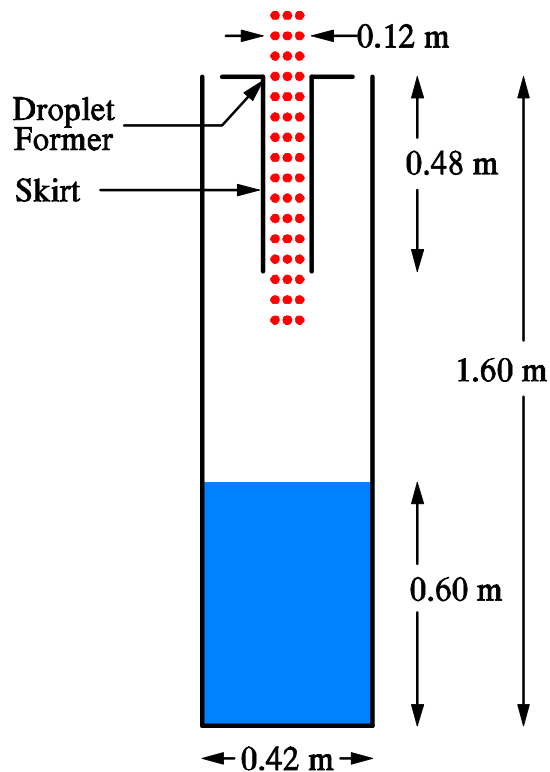


**Figure 7 Schematic of MIXA-6 as Modeled in IFCI**

#### 3.2 Incorporation of Pressurization in IFCI

The MIXA-6 experiment displayed an increase in pressure from an initial value of 0.1 MPa to a peak pressure of 0.13 MPa. This corresponds to an increase in the saturation temperature of approximately 7.5K. If the system were well stirred, this amount of subcooling would be more than enough to condense all of the steam measured in the experiment (Appendix B).

The IFCI code incorporates the effects of subcooling in its calculation of steam generation rate. It was therefore deemed necessary to include the pressurization of the test chamber in the calculation. This is done in IFCI by computing an effective flow area for the outflow boundary condition.

Order of magnitude estimates indicate that viscous drag on the walls of the vent tube was too small to explain the pressure drops measured in the MIXA-6 experiment. This means that the pressure drop is most likely due to kinetic losses at the entrance of the vent tube and at the throat in the vortex flowmeter. These types of pressure losses ( $\Delta P$ ) are usually modeled by the equation

$$\Delta P = K \rho_{\text{steam}} (\dot{Q}_{\text{steam}})^2; K = \frac{k}{2 A^2} \quad (3-1)$$

where  $\dot{Q}_{\text{steam}}$  is the volume flow rate of steam ( $\text{m}^3/\text{sec}$ ),  $A$  is the flow area of the pipe or component ( $\text{m}^2$ ),  $\rho_{\text{steam}}$  is the steam density ( $\text{kg}/\text{m}^3$ ), and  $k$  is a loss coefficient (dimensionless) that is a function of the geometry. The value for  $K$  in this analysis is derived from the published data for the MIXA-6 experiment.

The chamber pressure (Figure 8) and the steam volume flow rate (Figure 9) for MIXA-6 were published as separate curves in Reference 3. The curves, themselves, deserve some scrutiny. The time base for the pressure curve is the “time after the melt arrives at (the) water surface.” By comparison, the time when the melt arrives at the pool surface is clearly marked in Figure 9 between 0.3 and 0.35 seconds. This suggests that “time” in Figure 9 refers to the time after initial melt release. If these time axes are correctly labeled, then the peak pressure occurred approximately 0.32 seconds after the steam flow rate peaked. This might be possible if water were transported into the flowmeter, choking the flow of steam in the meter throat. Another possibility is that the time axis of the pressure

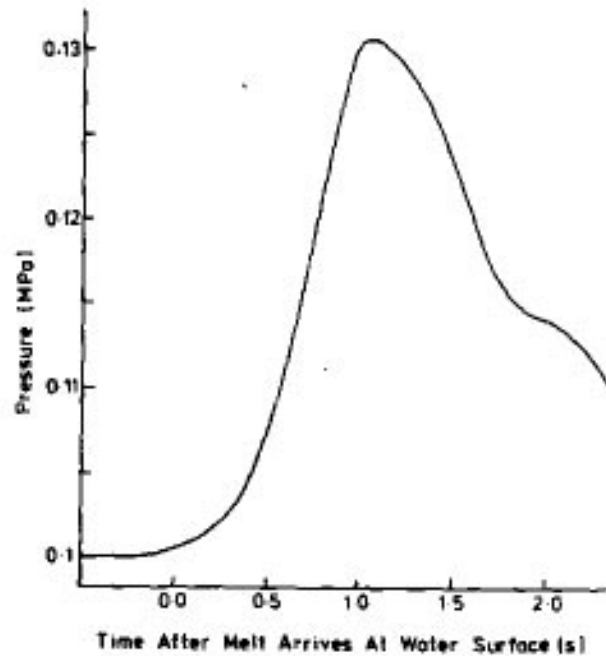


**Figure 8 The Measured Pressure in the Gas Space for Experiment MIXA-6**  
[copied from ref. 3]

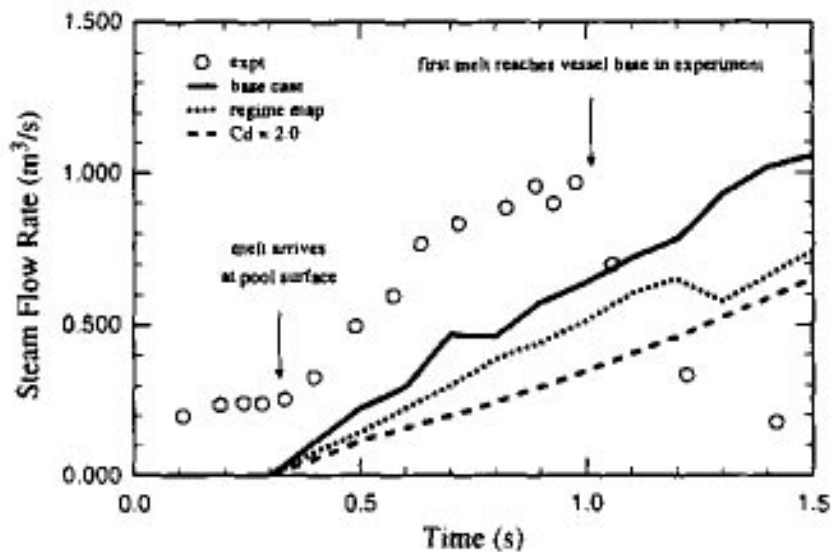


**Figure 9 The Transient Steaming Rate: A Comparison of the Calculated Values with the Experimental Data**  
[copied from ref. 3]

curve was mislabeled. If the time on the pressure curve were the time after the melt was released, then the peak pressure and the peak steam flow rate would correspond.

Both of these possibilities are plotted on the pressure-drop/flow-rate curve shown in Figure 10. The ordinate of this plot is the product of the steam density (based upon the pressure and assuming the saturation temperature) and the square of the steam volume flow rate. The abscissa is the difference between the pressure and the initial pressure. If the labels of the ordinates of Figure 8 and Figure 9 are correct then the curve labeled “unmodified” is appropriate. If the ordinate label of Figure 8 is incorrect, then the curve labeled “modified” is appropriate.

The initial behavior of both of these curves is consistent with equation 3-1. The pressure increase in both curves increases linearly with the product of mass flow rate and volume flow rate. The “unmodified” curve has a slope of  $8106 \text{ m}^{-4}$  for the first 0.65 seconds after the melt is released. The “modified curve” has an initial slope of  $40816 \text{ m}^{-4}$  for the first 0.89 seconds after the melt is released.

Both curves exhibit a behavior inconsistent with equation 3-1 as the steam flow rate decreases ( $>1.0$  seconds after the melt is released). Neither curve retraces itself as is expected. The “unmodified curve” shows the pressure drop to increase as the flow rate decreases. The “modified curve” shows the pressure drop nearly invariant during the same period of time. This suggests that something happened to the instrumentation during the experiment. One possibility

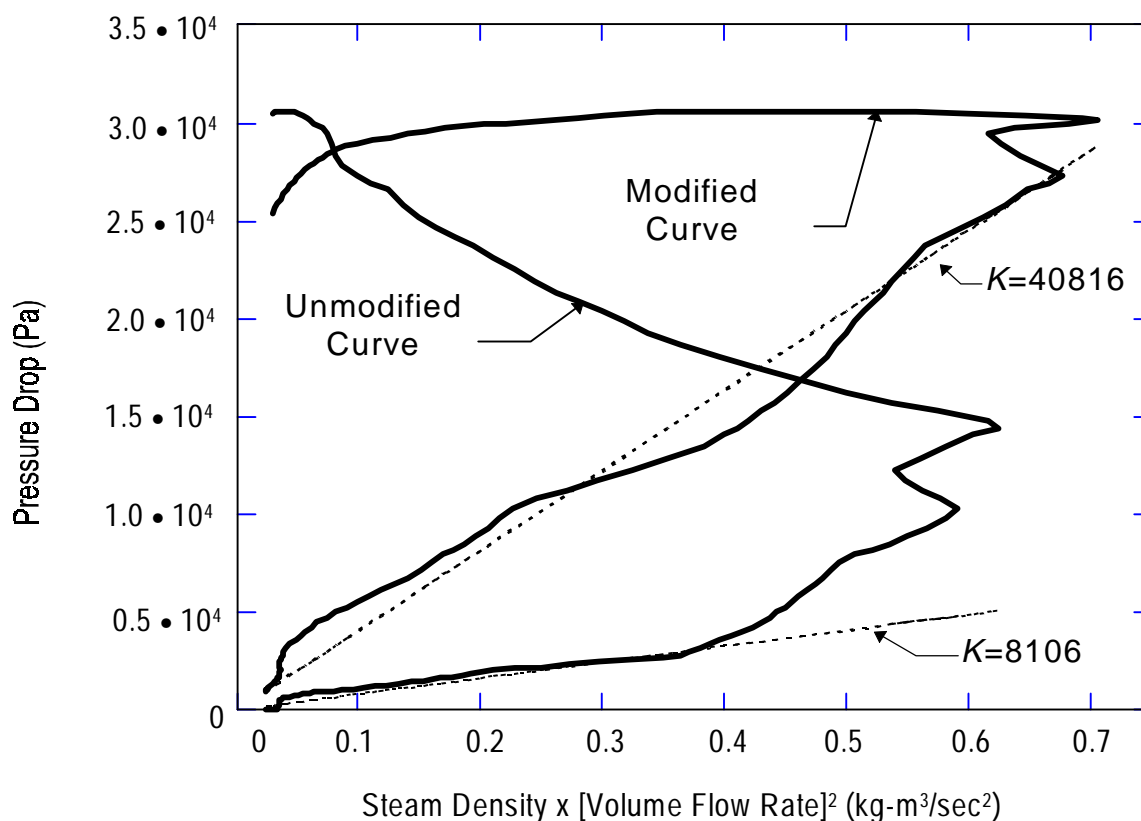


**Figure 10 Pressure-Drop/Flow-Rate Curve for the MIXA-6 Experiment**

is that water collected in the flowmeter. Another possibility is that the steam temperature increased. In either case, it suggests that the data may not be reliable after about 1 second.

In the absence of clarifying information<sup>1</sup>, the “modified curve” was chosen as the basis for calculating the outflow area used in the IFCI simulation. The pressure drop across the outflow boundary condition in IFCI is computed from the equation:

$$\Delta P = \frac{1}{(A_{exit,IFCI})^2} \rho_{steam} (\dot{Q}_{steam})^2 \quad (3-2)$$

The exit area used in IFCI ( $A_{exit,IFCI}$ ) is determined by comparing equation 3-2 to equation 3-1.

$$A_{exit,IFCI} = \frac{1}{\sqrt{K}} \quad (3-3)$$

Using this equation and the “corrected curve”, the outflow area to be used in IFCI is  $4.9497 \times 10^{-3} \text{ m}^2$ .

The exit area  $A_{exit,IFCI}$  should not be interpreted as a flow area actually occurring in the experiment. Pressure losses are expected to occur in two locations: at the entrance of the vent tube and at the throat in the vortex flowmeter. Each of these locations will have its own loss coefficient ( $k$  in equation 3-1). The implied loss coefficient used in IFCI is 2 (compare equations 3-1 and 3-2). Therefore the exit area used in IFCI,  $A_{exit,IFCI}$ , should be interpreted as a composite fitting coefficient derived from the measured pressure-drop/flow-rate curve.

### 3.3 Comparison of IFCI Predictions with Experimental Measurements

The IFCI predictions for steam generation rate (labeled as “IFCI Calculations with Subcooling”) are shown in Figure 11 with the data from the MIXA-6 experiment. IFCI clearly underpredicts the steam generation rate by approximately a factor of three. Only minor differences exist between the three meshes (11x36, 11x56, 11x96).

The experiment data, itself, suggests one reason for the disparity between measurement and prediction. The data clearly shows a significant steam generation rate before the melt hits the water. Since the volume of melt displacing the existing steam is relative small, this initial steam generation measurement can be attributed to only two effects: 1) heating of the steam by the melt falling through the steam, and 2) steam generation in the water due to radiation from the falling melt. Appendix D contains an order-of-magnitude analysis that shows that the latter of these two possibilities could easily account for the measurement. It is possible that both phenomena

---

<sup>1</sup> Brian Turland at Winfrith had been contacted about this anomaly. His investigations indicated that the published reports were consistent with the data logs. This information was not returned to us until the IFCI calculation had been completed. However, the IFCI calculations clearly underpredict the steam generation rate and, consequently, the pressurization. Therefore, the use of the “modified” curve rather than the “unmodified” curve is not expected to change the quality of the comparison with the data.

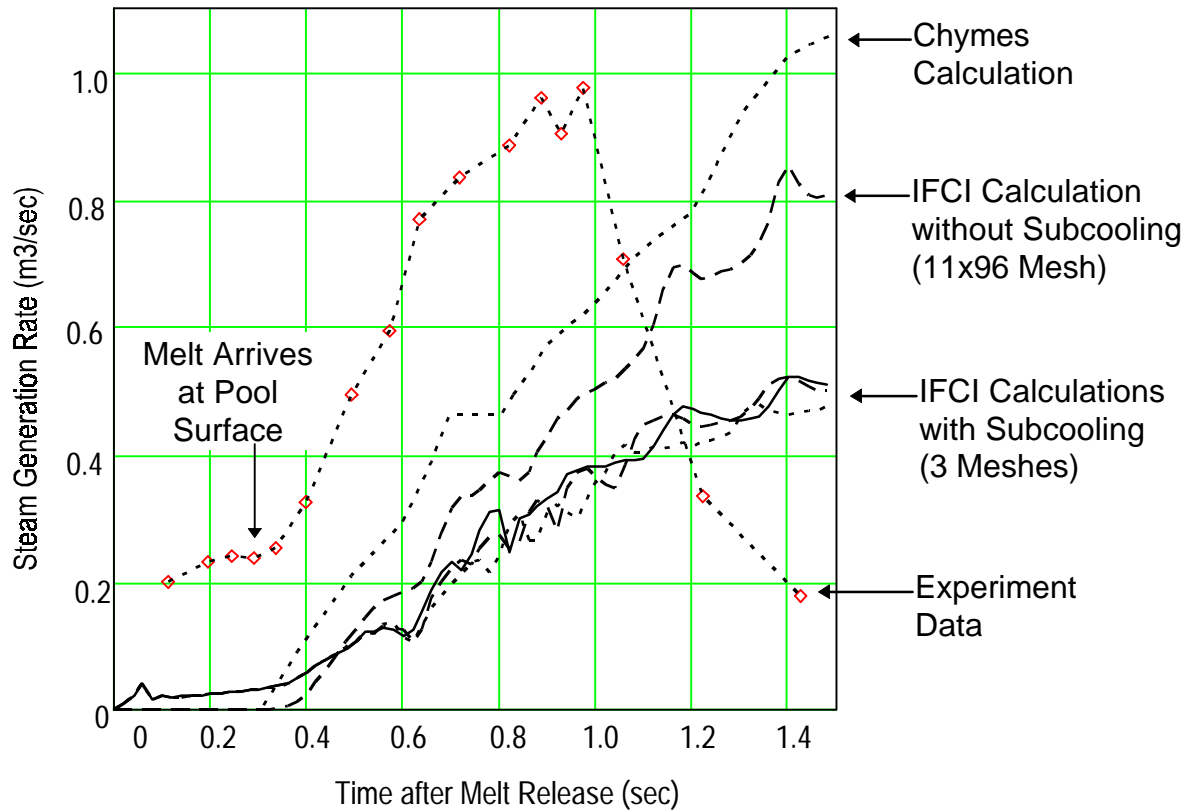


**Figure 11 Steam Production Rate Calculated by IFCI**

contribute to the observation. Neither is modeled in IFCI, which models radiation only within a cell.

Inter-cell radiation may also be necessary for the accurate description of heat transfer during coarse mixing. Currently, the radiative heat transfer between the melt and the water within a cell ( $E_{rad}$ ) in IFCI is modeled as:

$$E_{rad} = Area_{melt} \sigma (T_{melt}^4 - T_{water}^4) \alpha_{water} \quad (3-4)$$

where  $\alpha_{water}$  is the water volume fraction in that cell. While this is a reasonable estimate of the radiative heat transfer to the water within the cell, the total radiative loss from the melt should be independent of the cell water volume fraction. Physically, the balance of the radiative loss from the melt would be transferred to the water in adjacent cells. By neglecting this “inter-cell” radiation transport, IFCI underpredicts both the cooling rate of the melt and the consequent steam generation rate.

The case for an inter-cell radiation model is strengthened by an examination of the transmissivity of water. Table 2 shows the fraction of energy radiated by the melt that is absorbed by water. The absorbed fraction increases with the path length in the water and decreases with increasing melt temperature. The table indicates that approximately 60% of the energy radiated from a 3500 K source across a cell 20 mm wide (the radial cell size used in the IFCI analysis of MIXA-6) would

be absorbed by the water in that cell if the cell contained nothing but water. If the cell had only 50% water, then approximately 30% of the radiated energy would be absorbed in that cell with the balance being transmitted into the adjacent cell. These numbers suggest that the transmissivity of water should be included in an inter-cell radiation model in order to correctly predict the local steam generation rate.

Pressurization-induced subcooling also contributed to the low steam generation rate predicted by IFCI. In order to estimate the subcooling effects in the IFCI calculation of MIXA-6, the total heat transferred from the melt to the water was divided by the steam heat of vaporization and the steam density. This quantity is plotted in Figure 11 as “IFCI Calculation without Subcooling (11x96 mesh).” This curve is less than, but comparable to, the CHYMES (a fuel-coolant interaction code developed by Fletcher and Thyagaraja (1991) at AEA Culham Laboratory) prediction, which assumes saturated conditions. The difference between this curve and the IFCI calculations that include subcooling confirms that subcooling cannot be ignored.

The subcooling models in IFCI are, as yet, not assessed. It is clear that inter-cell radiation is important to the successful modeling of the MIXA-6 experiment, and that it will increase the predicted steam generation rate. An inter-cell model would also decrease the amount of subcooling in the vicinity of the melt, which would affect the predicted condensation rate. It is thus concluded that the subcooling models can be evaluated in experiments with high melt temperatures only after a reasonable inter-cell radiation model has been included in the calculation. The subcooling models could be better assessed using an experiment which utilizes hot solid spheres and, in which, the steam generation rate is measured. The relative low temperature of the solid spheres would minimize the radiation component of the heat transfer, and the absence of particle breakup would fix the particle surface area. It is possible that one of the QUEOS experiments [5] would be suitable. The authors are in contact with the QUEOS experimenters to determine if such an experiment has been conducted or is planned.

Table 2 The Fraction of Thermal Energy Absorbed as a Function of Melt Temperature and Path-Length (copied from ref. 4)

Path Length (mm)	Fraction of Incident Energy Absorbed		
	T=1000 K	T=2500 K	T=3500 K
1	0.967	0.599	0.343
10	1.	0.756	0.526
15	1.	0.786	0.560
20	1.	0.806	0.585
25	1.	0.822	0.604
30	1.	0.834	0.620

## 4. KROTOS-26 and KROTOS-38

### 4.1 Experiment Geometry

The KROTOS 26 and 38 experiments [6] were designed to obtain information on the shock propagation within a triggered fuel-coolant interaction. In the KROTOS-26 experiment, molten alumina was released into subcooled water and allowed to mix for approximately 2 seconds after the initial release. At that point, a high pressure gas container at the bottom of the water column was punctured, producing a pressure wave that propagated through the melt/water mixture. Pressure transducers located in the water column recorded the passage of the pressure wave after triggering. In the KROTOS-38 experiment, the fuel coolant interaction triggered spontaneously at approximately 1.3 seconds without the puncturing of the high pressure gas container.

The KROTOS 26 and 38 experiments differed primarily in the test-section diameter, the degree of subcooling, and the melt mass. The KROTOS-26 experiment was conducted in a water column that was 0.089 m in diameter. The test section for KROTOS-38 was 0.2 m in diameter. Additionally, the KROTOS-38 subcooling (79 K) was nearly twice the KROTOS-26 subcooling (40 K). Table 4 contains the experiment parameters specific to each experiment. Table 3 contains the locations of the pressure transducers.

**Table 4 KROTOS Experiment Parameters**

	<b>KROTOS 26</b>	<b>KROTOS 38</b>
Water depth	1.12 m	1.105 m
Melt mass	0.93 kg	1.533 kg
Melt Temperature	2573 K	2665 K
Water Temperature	333 K	294 K
Water column diameter	0.089 m	0.200 m

**Table 3 Pressure Transducer  
Locations**

<b>Transducer Number</b>	<b>Elevation in Water (mm)</b>	
	<b>KROTOS 26</b>	<b>KROTOS 38</b>
K0	0	0
K1	190	150
K2	390	350
K3	590	550
K4	790	750
K5	990	950

### 4.2 IFCI Calculations

In order to predict the effects of the trigger passing through the alumina/water mixture, IFCI must calculate the falling and coarse mixing that precedes the trigger. Attempts to perform this calculation have only been partially successful. With all code models turned on, IFCI calculated the KROTOS-26 mixing stage to about 0.35 seconds. With the condensation model turned off, IFCI calculated the KROTOS-26 mixing stage to 1.48 seconds before the time step became impossibly small. This suggests that there is something about the condensation process that IFCI does not yet handle well.

In order to confirm that the problem was not a function of the specific KROTOS-26 geometry, the KROTOS-38 mixing was also calculated. To further differentiate the analyses, the melt was introduced into the IFCI model as an inflow condition (Appendix E). It was felt that this would

present less severe numerical conditions than the initial cylinder of melt modeled in KROTOS-26 (Figure 12). Unfortunately, the results of the KROTOS-38 mixing calculation were substantially the same as those for KROTOS-26: water subcooling presents a numerical problem for the IFCI code. The problem has been associated with a bad solution in the pressure iteration in which there is a small amount of gas. Further investigation will be necessary to solve the problem.

Even though the condensation had to be turned off to run the KROTOS-26 prediction out to 1.48 seconds, it is still interesting to examine the results. The left side of Figure 13 shows the predicted melt volume fraction at 1.48 seconds. The right side shows the liquid volume fraction at the same time. The lower set of arrows indicate the initial water level in the experiment (1.12 m). The upper set of arrows indicate the water overflow level (1.035 m, see Figure 12). The x-axes of the plots are the radial coordinates with the centerline at the left edge. The height-to-width dimensions in Figure 13 are distorted, but are correct in Figure 12.

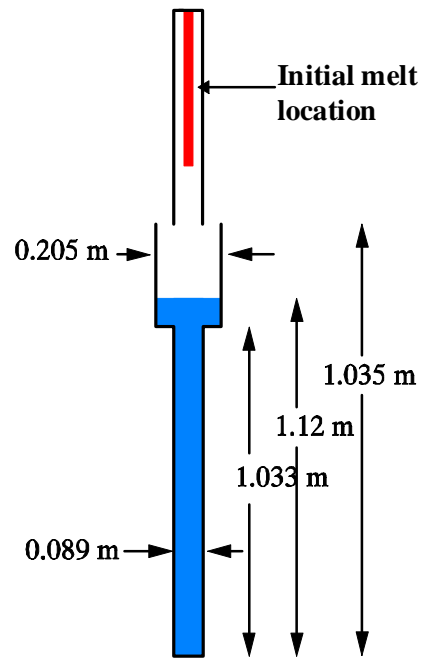


**Figure 12 Schematic of KROTOS-26 as Modeled in IFCI**

The map of melt volume fraction shows that the melt has descended about 3/4 of the distance to the bottom on the outer periphery. The melt has not penetrated as far in the center. This is because the vapor is rising in the center and is helping to levitate the melt in the center region. A considerable amount of molten material appears to have accumulated on the shoulder at an elevation of 1.033 m (see Figure 12 to identify location of shoulder).

The map of the liquid region indicates the presence of vapor through about 3/4 of the water region. Vapor that is generated at the periphery of the test section is migrating radially inward where there is no melt present. Some water has reached the overflow level, and is spilling out of the test vessel.

The pressure transducer recordings of the trigger and resulting fuel-coolant interaction [6] give some clue as to the state of the coarse mixing at the time of triggering (2 sec). The trigger is initiated at about 7.4 ms as indicated by the K0 trace (Figure 14). The pressure wave travels past the K1, K2, and K3 transducers before 8 ms. The fuel/coolant interaction appears to originate at or above the K5 transducer. The resulting explosive pressure wave then travels back downward until it reaches the bottom of the water (K0).

Calculated arrival times for the initial pressure wave at various transducers are indicated on the plot by vertical dotted lines (labeled ts1 through ts5). These times are based on an acoustic



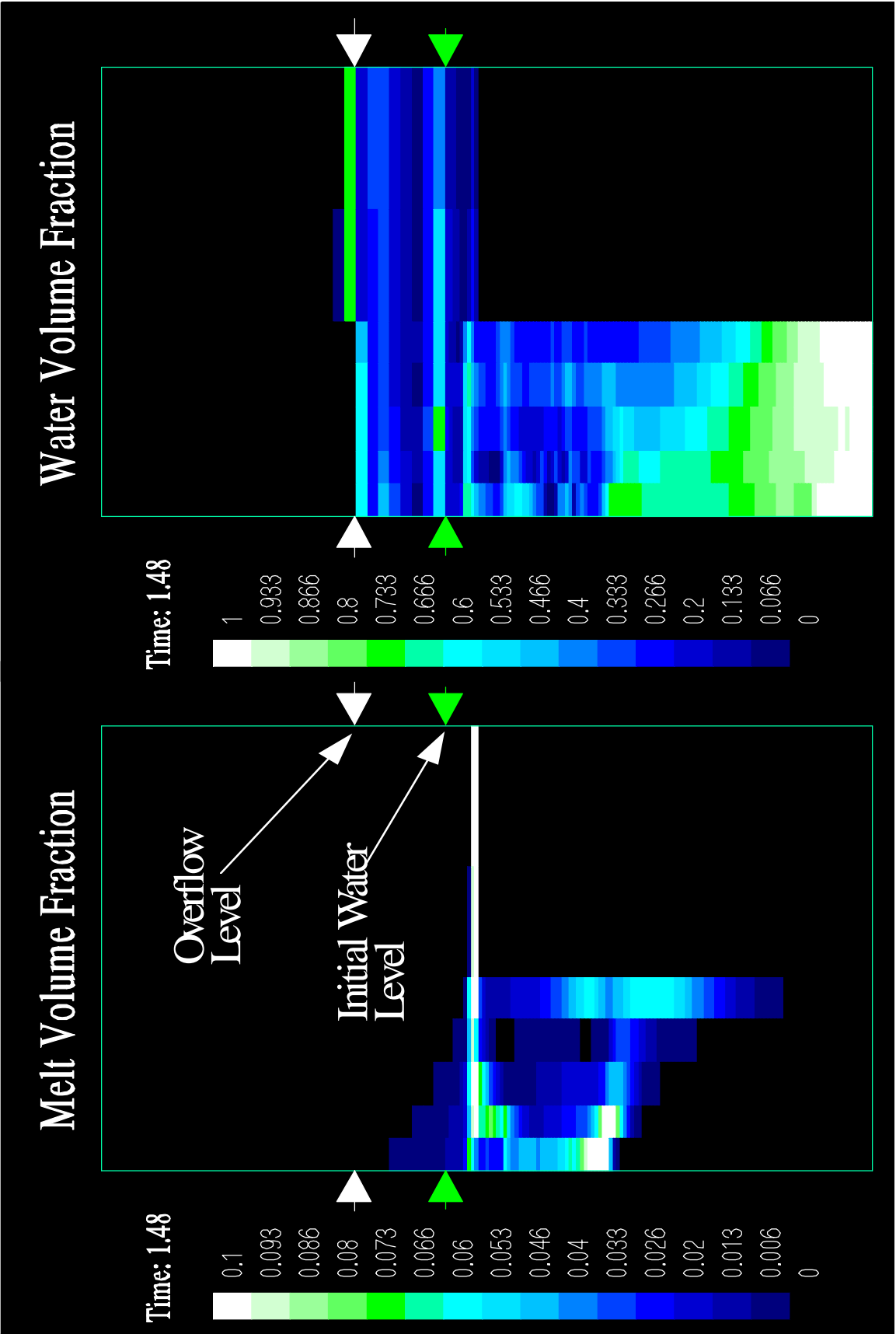
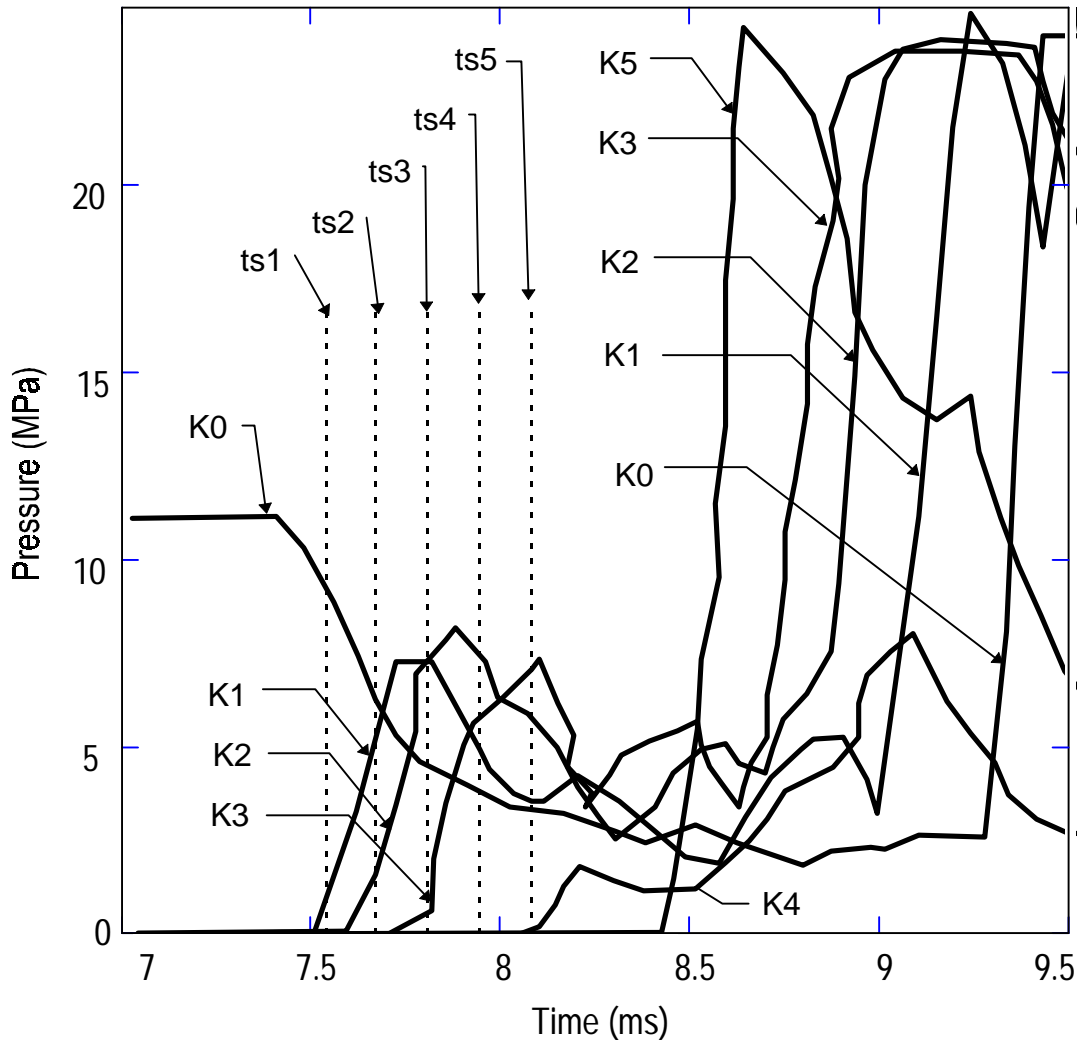


Figure 13 IFCI Mixing Predictions for KROTOS-26 (1.48 sec, no condensation)



**Figure 14 Post-Triggering Pressure Transducer Readings from KROTOS-26**

velocity of 1476 m/second. These calculated passage times correspond reasonably well to the measured pressure waves for the K1, K2, and K3 transducers. They precede considerably the measured pressure waves for the K4 and K5 transducers. Since the acoustic velocity is highly sensitive to the presence of gas in the system, it may be concluded that little steam existed below the level of the K3 transducer.

Since IFCI was unable to deal with the subcooling in the KROTOS experiments, a simplified mixing geometry was created as the initial condition for a detonation calculation. For this calculation, the water region was divided into two sections. The region between the bottom of the test section and an elevation of 0.69 m (containing gauges K1, K2, and K3) was assumed to be 99.9% water<sup>2</sup>. This is consistent with the measured velocity of the pressure wave in this region. Between an elevation of 0.69 m and 1.12 m (containing gauges K4 and K5), a mixture of

<sup>2</sup> A small amount of steam is added to water regions at the start of a calculation in order to enhance numerical stability.

2% melt, 20% vapor, and 78% water was assumed. The choice of volume fractions was arbitrary, but in the same range of values computed for MAGICO-701 and MIXA-6 experiments. The high-pressure trigger used in the KROTOS-26 experiment was included in the calculation. The results are shown in Figure 15. The responses of the K1, K2, and K3 gauges are approximately the same as those measured in the experiment (Figure 14). The K3 transducer begins to respond within 0.5 ms after the initiation of the trigger.

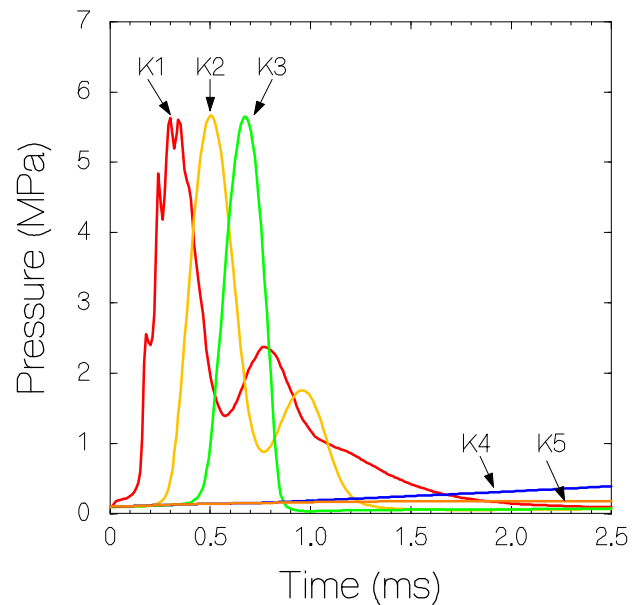


**Figure 15 Predicted Response to the Detonation Trigger**

The similarity between prediction and measurement does not extend to the mixing zone in which the K4 and K5 transducers are located. The K4 gauge responds only slightly to the incoming pulse and the K5 gauge does not respond at all (Figure 15). It is clear that the triggering pulse is predicted to die out in the mixing zone. Additional calculations in which a single cell is “forced” to trigger fail to show either a pressure rise of the correct magnitude or any sign of propagation. This is due to the predicted condensation and compression of steam in the mixing zone.

The fact that the KROTOS-26 experiment was successfully triggered means that one of two conditions must have existed in the experiment. Either the average steam volume fractions was significantly lower than 20 %, or there was a steam-free water zone adjacent to the location of initial detonation. Since IFCI cannot successfully deal with substantial amounts of subcooling at this time, the first of these possibilities cannot be examined. However, 20% steam is not exceptionally large for saturated conditions where detonations also occur.

The second possibility involving a water channel is intriguing, and there are a number of features in the detonation data that are consistent with such a configuration. First, the detonation wave is downward propagating from the K5 transducer. The K4 transducer registers a delayed response to the pressure pulse, but the detonation origin is clearly closer to the K5 transducer, since it is the first to register the FCI. This suggests that the triggering pulse passed the K4 transducer, which had vapor in the vicinity, and initiated a detonation at a higher elevation. Had the pulse passed through a region with a significant vapor fraction, it would have probably damped out. The fact that it was strong enough to initiate a detonation suggests that it traveled along a water channel.

The second feature that suggests a water channel is the speed of the detonation wave. The transit time of the shock between the K5 and the K0 transducers is approximately 0.8 ms. This compares to the calculated transit time of 0.67 ms. If there were significant amounts of vapor

along the shock path, the transit time would probably be much longer and the peak pressures would display significant damping.

Finally, a water channel could explain the response of the K4 transducer to the detonation. The magnitude of the detonation wave recorded by K4 is much smaller than recorded by both K5 and K3. It is unlikely that the magnitude of the detonation wave dropped at K4 and then increased by the time that it arrived at K3. It is more likely that the detonation was damped by a mixing zone adjacent to the transducer but not extending completely to the center of the test section.

If the water channel hypothesis is correct, it could have broad implications about the physics of fuel coolant interactions. It would suggest that detonations propagate on the periphery of mixing zones and penetrate a finite distance into the zone. The penetration distance would be a function of the component volume fractions at the periphery. Fuel not located within the penetration zone would not participate in the detonation. This would account for the thermodynamic inefficiency of most FCI's.

## 5. Single Droplet Oxidation Experiment

Nelson and Duda designed a series of experiments to examine the physics of triggering by photographing the behavior of a single drop when a pressure wave of known strength passed over the drop.[7, 8] In these experiments, a single droplet of material was melted approximately 20 mm above a pool of water. The molten drop was then released into the pool and allowed to sink to a specified depth. A pressure pulse was then generated at the bottom of the water pool and the resulting interaction with the droplet was recorded with a high-speed movie camera. From this, threshold triggering strength as a function of water temperature, system pressure, melt temperature, and melt composition was determined.

The effects of oxidation on triggering were examined by varying the initial oxygen content [9]. To better understand the impact of oxidation on triggering, the bubble growth around an oxidizing iron droplet was photographed. The bubble size was measured and compared to the bubble size of a non-oxidizing droplet ( $\text{FeO}_{1.2}$ ) in order to determine the extent of oxidation. The results of this measurement were reported in reference 10 and are summarized in Table 5.

Table 5 Initial Conditions and Results for the Single Droplet Test

Droplet Composition	Fe
Droplet Mass	500 mg
Initial Droplet Temperature	1800 K
Droplet Fall Velocity	0.58 m/sec
Coolant Composition	water
Coolant Bulk Temperature	298 K
Reaction Time	75 msec
% of Fe Reacted (assuming FeO reaction)	0.09

The IFCI code contains three parabolic-rate models for iron oxidation. Equations (5-1) [11,12,10] and (5-2) [13,12,10] were developed by White. Equation (5-3) was developed by Baker [14,10].

$$w^2 = 1.4 \cdot 10^{11} t \exp(-90800 / RT) \quad (5-1)$$

$$w^2 = 2.4 \cdot 10^{12} t \exp(-84350 / RT) \quad (5-2)$$

$$w^2 = 2.449 \cdot 10^6 t \exp(-50000 / RT) \quad (5-3)$$

Parabolic rate equations imply that the primary limiting transport mechanism is oxygen diffusion through the oxide created at the outer surface of the material. In these equations,  $w$  is the weight of oxygen consumed in  $\text{mg-O/cm}^2$  of oxidizing surface,  $t$  is time in seconds,  $R$  is the universal gas constant (1.986 cal/mole-K), and  $T$  is the material temperature in K. They also imply an isothermal condition and a 1-D Cartesian geometry. They have been appropriately modified for the spherical geometry and variable temperature of the molten fuel in IFCI. Provisions are also made in IFCI for oxidation rate limitations due to steam availability and steam-hydrogen counter-diffusion in the boundary layer.

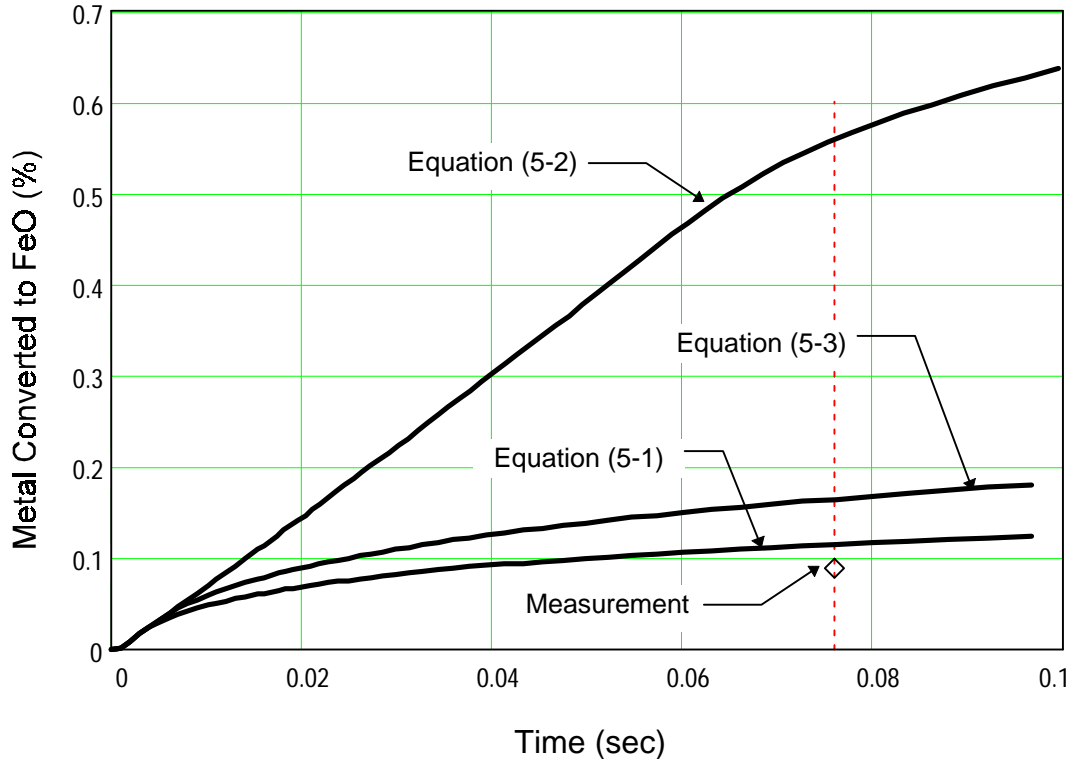
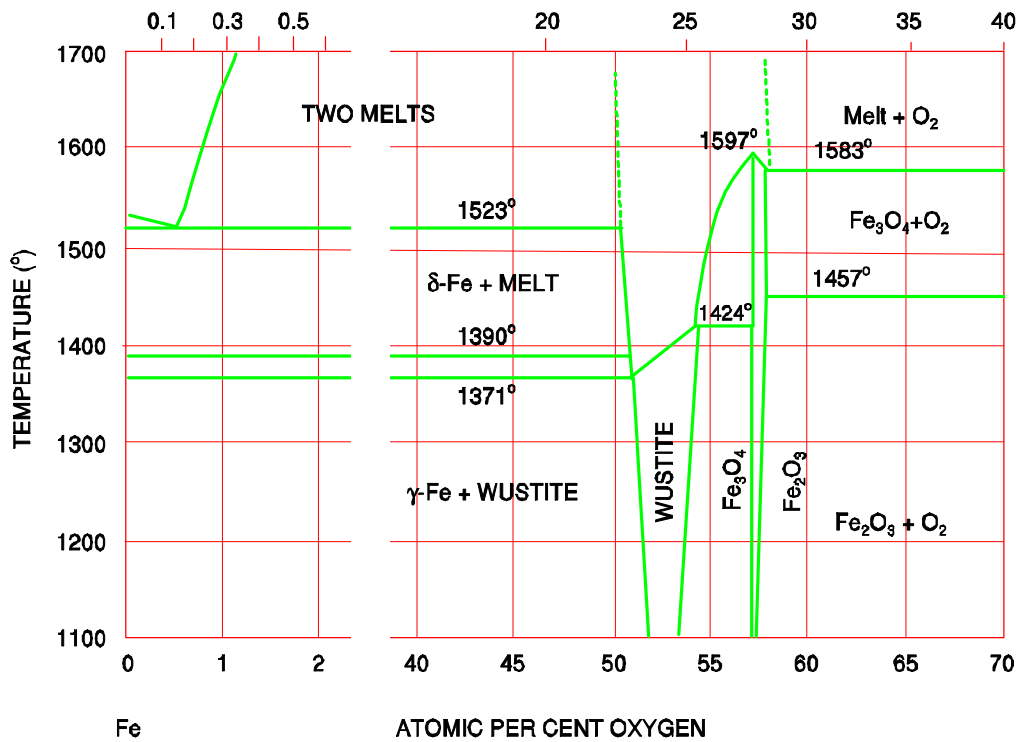


**Figure 16 IFCI Oxidation Predictions**

The IFCI predictions for the oxidation experiment are shown with the actual measurements in Figure 16. The vertical axis on this graph is the percentage of the 500 mg iron drop that is oxidized. The horizontal axis is the oxidation time. Predictions based upon all three correlations are shown along with the measured oxidation level at 0.076 seconds (the diamond). Of the three correlations, equation (5-1) displays the best agreement with experimental measurement (0.12% vs. 0.09%). Equation (5-3) predicts approximately twice the measurement (0.16%). For both of these cases, the oxidation rate is unaffected by the availability of steam. The diffusion through the oxide layer is the controlling factor.

The use of equation (5-2) produces an oxidation prediction that is much too large. In fact, the first 0.07 seconds of the reaction is controlled by the availability of steam. It is only after this point that the oxide layer becomes the limiting factor. Use of this equation is therefore discouraged.

While the agreement between IFCI and the data is encouraging, it should be pointed out that a larger class of oxidation problems has not been addressed. Specifically, above a certain temperature, an oxide layer will not form until the outer surface of the droplet cools sufficiently. The problem is more clearly described by referring to the iron/oxygen phase diagram (Figure 17). The diagram shows that the temperature range over which molten iron can coexist with wustite is from 1371°C to 1424°C. Between 1424°C and 1597°C, the oxide layer will be  $\text{Fe}_3\text{O}_4$ . Above 1597°C, an oxide layer will not form. Above this temperature, the oxygen uptake will be limited by either oxygen diffusion in the liquid iron or effects in the surrounding gas bubble. IFCI



Fe  
Figure 17 Iron/Oxygen Phase Diagram (Ref. 15)

accounts only for the gas-bubble effects and does not account for diffusion within the liquid iron. Although the diffusivity of the liquid iron is expected to be greater than that of the oxides, it is not clear that the gas layer effects would truly be the limiting factor in the oxidation process.

Even if the gas layer effects are found to be the limiting factor in these types of circumstances, the reliability of the oxidation will remain less certain than the case when the oxidation is oxide-limited. The gas layer dimensions surrounding the fuel droplet reflect the lack of any in-depth studies of the flow fields. As such, predictions of oxidation where the melt temperature exceeds the maximum oxide temperature must be viewed as educated guesses.

The appropriateness of this concern to prototypic fuel-coolant reactions must be judged with respect to the melt source configuration. The maximum oxide temperatures of iron and zirconium are 1870 K and 2973 K. The melting temperature of urania is 3113 K. If either iron or zirconium are raised to the urania melting temperature, then oxygen can be dissolved into the metal unrestricted by an oxide skin. Under these conditions, the model comparison presented in this report would be inapplicable.

## 6. Conclusions

It should be noted at the onset that all of the experiments chosen for this validation exercise are integral in nature and, as such, cannot be used to validate isolated models within the IFCI code. For example, one cannot examine the melt breakup model by comparing the MAGICO experiments to the MIXA experiments. The quantities measured in each experiment are different and are, themselves, the result of many physical process. These processes include film boiling in two-phase flows, particle drag in two-phase flows, and radiative heat transfer in heterogeneous regions, among others. The differences between the MIXA and MAGICO experiments are due to differences in all of these processes as well as the difference in melt breakup. Using a set of experiments that is progressively more complicated is, nonetheless, helpful to the validation process. For example, a critical examination of predicted quantities such as melt front velocity is helped by absence of particle breakup in the MAGICO experiment.

To date, the most insightful exercise has been the comparison between IFCI and the MIXA-6 experiment. While the exercise raises several questions, it does indicate a very clear requirement: inter-cell radiation must be added to any fuel/coolant interaction code in order to handle the MIXA-6 experiment, or any experiment that uses prototypic (i.e., high temperature) melts. Radiation transport from falling melt to the water pool can clearly induce steam generation.

The importance of inter-cell radiation is also demonstrably important to steam generation during the coarse mixing process. Regions which become water-deficient become partially “transparent”, and radiative heat transfer to water-rich regions will evolve. The net result will be a higher steam generation rate and a faster melt cooling rate. This will also have some effect on the calculated impact of subcooling; subcooled water adjacent to hot melt will be radiatively preheated before it comes into actual contact with the melt. All of these effects will be most pronounced in the outer zone of the mixing region, where the melt-water ratios are more conducive to FCI’s.

There is a tendency for IFCI to underpredict the amount of time that it takes the melt to reach the bottom of the test chamber. This was observed in both the MAGICO-701 and KROTOS-26 experiments. This trait deserves some attention since one of the more common triggers appears associated with this event. If the melt arrival time is underpredicted, the amount of melt present at the time of triggering may also be underpredicted.

Studies presented in this paper (Appendix A) demonstrate the connection between numerical diffusion and early arrival times for single phase flows. However, the results of the MIXA-6 two-phase calculations were not as sensitive to grid refinement as were the single-phase studies. One possible explanation is that the drag correlations applied to the melt need improvement. IFCI uses single-phase drag correlations that are modified for two-phase flows in an ad-hoc fashion that has not been validated. More study is needed to determine if this improvisation has a significant effect on the melt arrival time. Another possibility is that the meshes must be refined even more for two-phase flow than for single-phase flows. Further 1-D calculations with two-phase flows, similar to those already conducted for single-phase flows should shed some light on this possibility.



The oxidation model in IFCI successfully predicted the results of a single-drop steel oxidation experiment. The influence of numerical diffusion on this calculation was avoided by modeling the water as a single water cell. Calculations of more prototypical oxidation scenarios will include particle breakup during coarse mixing. Therefore, the overall success of prototypical oxidation predictions will depend on the accuracy of the coarse mixing models.

Attempts to model the mixing in the KROTOS-26 and KROTOS-38 experiments have been unsuccessful so far. The problem has been associated with a bad pressure solution that the code produces. The bad solution seems to occur in certain cells in which small amounts of vapor coexist with hot fuel. The problem is more likely to arise when the problem contains significant subcooling. Further study is necessary to fully diagnose and solve the problem.

IFCI was used to examine the propagation of the triggering wave in the KROTOS-26 experiment. A simplified 2-zone mixing configuration was used in which the lower zone was occupied solely by water and the upper zone was occupied by a reasonable mixture of fuel, vapor, and water. The propagation of the triggering pulse through the lower zone was well modeled by IFCI. However the triggering pulse was predicted to die out in the multiphase zone. This led to a closer examination of the detonation data and the conclusion that the mixing zone in the KROTOS-26 is probably not one-dimensional. This further accentuates the need for a mixing calculation that can examine this possibility.

The question of future directions naturally presents itself at this point. A code such as IFCI must perform as both an experiment analysis tool and a predictive tool for prototypical accidents. The experiment analyses presented in this document are illustrative of the first function. The process of model assessment naturally promotes a close scrutiny of both experiment data and experiment design. It is frequently found that a more intimate knowledge of the physics operative in an experiment is a byproduct of the attempt to model the experiment. The analyses of the MAGICO-701 and MIXA-6 experiments are examples of this. In facilitating a better understanding of existing experiments, IFCI may be helpful in designing future experiments.

In principle, IFCI should be able to extrapolate the current state of FCI knowledge gained from small scale experiments to prototypical conditions. Some work will be required to debug the "surface tracker" model, which enables IFCI to model melt jets having a diameter greater than the cell width. This feature will probably be necessary for many prototypical scenarios.

While the potential of IFCI has been demonstrated in this document, it is clear that the code must be improved. First, the numerical problems associated with subcooling must be solved in order to address both detonation experiments and prototypic accident scenarios. Next, an inter-cell radiation model must be added in order to correctly predict the steam generation rate and the correct steam/water/fuel proportions. Finally, the subcooling models should be assessed against an experiment which does not involve significant amounts of radiation transport. With these improvements, IFCI has the potential of resolving the structure of coarse mixing and consequently, producing a greater understanding of propagating detonations.

## 7. References

1. T. G. Theofanous, W. W. Yuen, S. Angelini, X. Chen, W. H. Amarasooriya, and S. Medhekar, Steam Explosions: Fundamentals and Energetic Behavior, NUREG/CR-5960, Department of Chemical and Nuclear Engineering, Center for Risk Studies and Safety, University of California at Santa Barbara (1994).
2. M. K. Denham, A. P. Tyler, and D. F. Fletcher, "Experiments on the Mixing of Molten Uranium Dioxide with Water and Initial Comparisons with Chymes Code Calculations," Proceedings of the Fifth International Topical Meeting on Reactor Thermal Hydraulics (NURETH-5), Vol VI, Salt Lake City, Ut, USA (September 21-24, 1992).
3. D. F. Fletcher and M.K Denham, "Validation of the Chymes Mixing Model," presented at the CSNI Specialist meeting on Fuel-Coolant Interactions, Santa Barbara, USA, (January 5-8, 1993)
4. D. F. Fletcher, Assessment and Development of the Bankoff and Han Coarse Mixing Model, CLM-R252, Culham Laboratory, Abingdon (1985).
5. L. Meyer and G. Schumacher, QUEOS, a Simulation-Experiment of the Premixing Phase of a Steam Explosion with Hot Spheres in Water, FZKA Report 5612, Forschungszentrum Karlsruhe, (in press).
6. H. Hofmann, et. al., Krotos 26 to Krotos 30: Experimental Data Collection, Technical Note No. I.92.115, Joint Research Centre Safety Technology Institute (Nov. 1992).
7. L. S. Nelson and P. M. Duda, Steam Explosion Experiments with Single Drops of Iron Oxide Melted with A CO<sub>2</sub> Laser, NUREG/CR-2295, SAND81-1346, Sandia National Laboratories, Albuquerque, New Mexico (1981).
8. L. S. Nelson and P. M. Duda, Steam Explosion Experiments with Single Drop of Iron Oxide Melted with a CO<sub>2</sub> Laser; Part II. Parametric Studies, NUREG/CR-2718, SAND82-1105, Sandia National Laboratories, Albuquerque, New Mexico (April, 1985).
9. L. S. Nelson and P. M. Duda, "Steam Explosions of a Metallic Melt as its Degree of Oxidation Increases: Fe, FeO<sub>1.0</sub>, and FeO<sub>1.2</sub>," Proc. Int'l Mtg. on Thermal Nuclear Reactor Safety, Aug. 29-Sept. 2, 1982, Chicago, IL, U.S. Nuclear Regulatory Commission, Washington, D. C., NUREG/CP-0027, v.2, 981-986.
10. L. T. Pong, A Theoretical Study of the Reactions of Molten Zr, Fe, and Al With Water, SAND88-7119, Sandia National Laboratories, Albuquerque, New Mexico (October 1988).
11. J. F. White, *et. al.*, GEMP-5A, p55 (1966).

12. D. A. Powers, Chapter 4 in Core-Meltdown Experimental Review, SAND74-0382, NUREG-0205, Sandia National Laboratories (March 1977).
13. J. F. White, *et. al.*, in Seventh Annual Report-AEC Fuel and Materials Development Program, GEMP-1004 (March 1968).
14. L. Baker, Jr., "Hydrogen-Generating Reactions in LWR Severe Accidents", Proceedings of the International Meeting on LWR Severe Accident Evaluation, Cambridge, MA (August 1983).
15. M. Hansen and K. Anderko, Constitution of Binary Alloys, McGraw-Hill Book Company, New York (1989).
16. F. J. Davis and M. F. Young, Integrated Fuel-Coolant Interaction (IFCI 6.0) Code User's Manual, NUREG/CR-6211, SAND94-0406, Sandia National Laboratories, Albuquerque, New Mexico (April 1994).
17. J. H. Keenan, *et. al.*, Steam Tables, John Wiley and Sons, New York (1978).
18. Personal communication from Brian Turland, Winfrith, to Fred Davis, Sandia National Laboratories, (October 18, 1994).
19. Robert Siegel and John R. Howell, Thermal Radiation Heat Transfer, McGraw-Hill Book Company, New York (1972).
20. S. Angelini, W.W. Yuen, and T.G. Theofanous, "Premixing-Related Behavior of Steam Explosions," Nuclear Engineering and Design, vol. 155 (April, 1995).